AGU ADVANCING EARTH AND SPACE SCIENCES

Geophysical Research Letters

RESEARCH LETTER
10.1029/2024GL110131

Meltwater Orientations Modify Seismic Anisotropy in Temperate Ice

Cassandra Seltzer[1], **Maria-Gema Llorens**[2], **and Andrew J. Cross**[3]

[1]Department of Earth, Atmospheric, and Planetary Sciences, Massachusetts Institute of Technology, Cambridge, MA, USA, [2]Geosciences Barcelona (GEO3BCN-CSIC), Barcelona, Spain, [3]Department of Geology and Geophysics, Woods Hole Oceanographic Institution, Woods Hole, MA, USA

Key Points:

- We used simulations of deforming temperate ice to show that the alignment of interstitial meltwater changes bulk seismic properties
- The amount of melt required to significantly modify seismic properties is at least 50% lower than previously reported
- Melt should be considered when using seismic and radar anisotropy to interpret viscous ice deformation and enhancement

Supporting Information:

Supporting Information may be found in the online version of this article.

Correspondence to:

C. Seltzer,
cseltz@mit.edu

Citation:

Seltzer, C., Llorens, M.-G., & Cross, A. J. (2024). Meltwater orientations modify seismic anisotropy in temperate ice. *Geophysical Research Letters*, *51*, e2024GL110131. https://doi.org/10.1029/2024GL110131

Received 3 MAY 2024
Accepted 21 JUN 2024

Abstract Seismology is increasingly used to infer the magnitude and direction of glacial ice flow. However, the effects of interstitial meltwater on seismic properties remain poorly constrained. Here, we extend previous studies on seismic anisotropy in temperate ices to consider the role of melt preferred orientation (MPO). We used the ELLE numerical toolbox to simulate microstructural shear deformation of temperate ice with variable MPO strength and orientation, and calculated the effective seismic properties of these numerical ice-melt aggregates. Our models demonstrate that even 3.5% melt volume is sufficient to rotate fast directions by up to 90°, to increase Vp anisotropy by up to +110%, and to modify Vs anisotropy by −9 to +36%. These effects are especially prominent at strain rates $\geq 3.17 \times 10^{-12}$ s^{-1}. MPO may thus obscure the geophysical signatures of temperate ice flow in regions of rapid ice discharge, and is therefore pivotal for understanding ice mass loss.

Plain Language Summary Ice on Earth is pulled toward the sea by gravity, contributing to global mean sea level rise. To better understand the flow, or movement, of ice at the continent scale, geophysical surveys are increasingly being used to measure the microscopic alignment ("fabric") of ice crystals, since ice with a strong fabric flows more readily. However, in temperate regions close to the ice melting point, melt pockets may also become aligned, creating additional macroscopic geophysical signatures. Here, we use numerical simulations to examine the combined effects of ice crystal fabric and melt alignment on the geophysical (seismic) properties of ice containing small amounts of melt. We show that melt can change the seismic fast direction (related to the inferred flow direction) of ice by up to 90°, particularly as the volume of melt exceeds 3.5%, and that different melt orientations can either enhance or diminish the anisotropy-based estimates of flow that some studies use to predict ice mass loss. These effects are especially prominent in faster-flowing ice, highly relevant to ice mass loss in warming regions. Geophysical studies that do not account for melt orientation may therefore produce incorrect estimates of flow, leading to inaccuracies in future climate models.

1. Introduction

Land ice loss is the dominant driver of global mean sea level rise, and is projected to further increase over the coming century and beyond (Oppenheimer et al., 2019). However, ice dynamics remain the largest source of uncertainty in forward models of sea level rise (Bamber et al., 2019; Edwards et al., 2021; Li et al., 2023). As such, there is a pressing need to further constrain the past and present behavior of Earth's polar ice sheets and glaciers, beginning with observations of viscous flow.

It is well established that ice exhibits strong viscous anisotropy. For a given strain rate, ice single crystals deform up to 60 times more readily when oriented to maximize shearing on their crystallographic basal plane (Duval et al., 1983). Thus, viscoplastic ice flow commonly produces a crystallographic preferred orientation (CPO)—also referred to as crystal orientation fabric (COF)—due to the progressive alignment of ice basal planes (Azuma & Higashi, 1985; Fan et al., 2020; Figures 1a and 1b). In ice polycrystals, CPO evolution is often associated with strain weakening (e.g., Fan et al., 2021), termed "enhancement," with deformation becoming up to 10 times easier in orientations favorable for basal slip (Pimienta et al., 1987; Treverrow et al., 2012). It is therefore desirable to determine both the intensity and orientation of natural ice CPO.

Early efforts to characterize ice sheet microstructure were centered largely around drilling at ice divides and ice domes (see Faria et al., 2014 for a historical overview). These studies provide only a local view of ice sheet anisotropy, whereas regional CPO measurements are needed for the development of more accurate ice flow

10.1029/2024GL110131

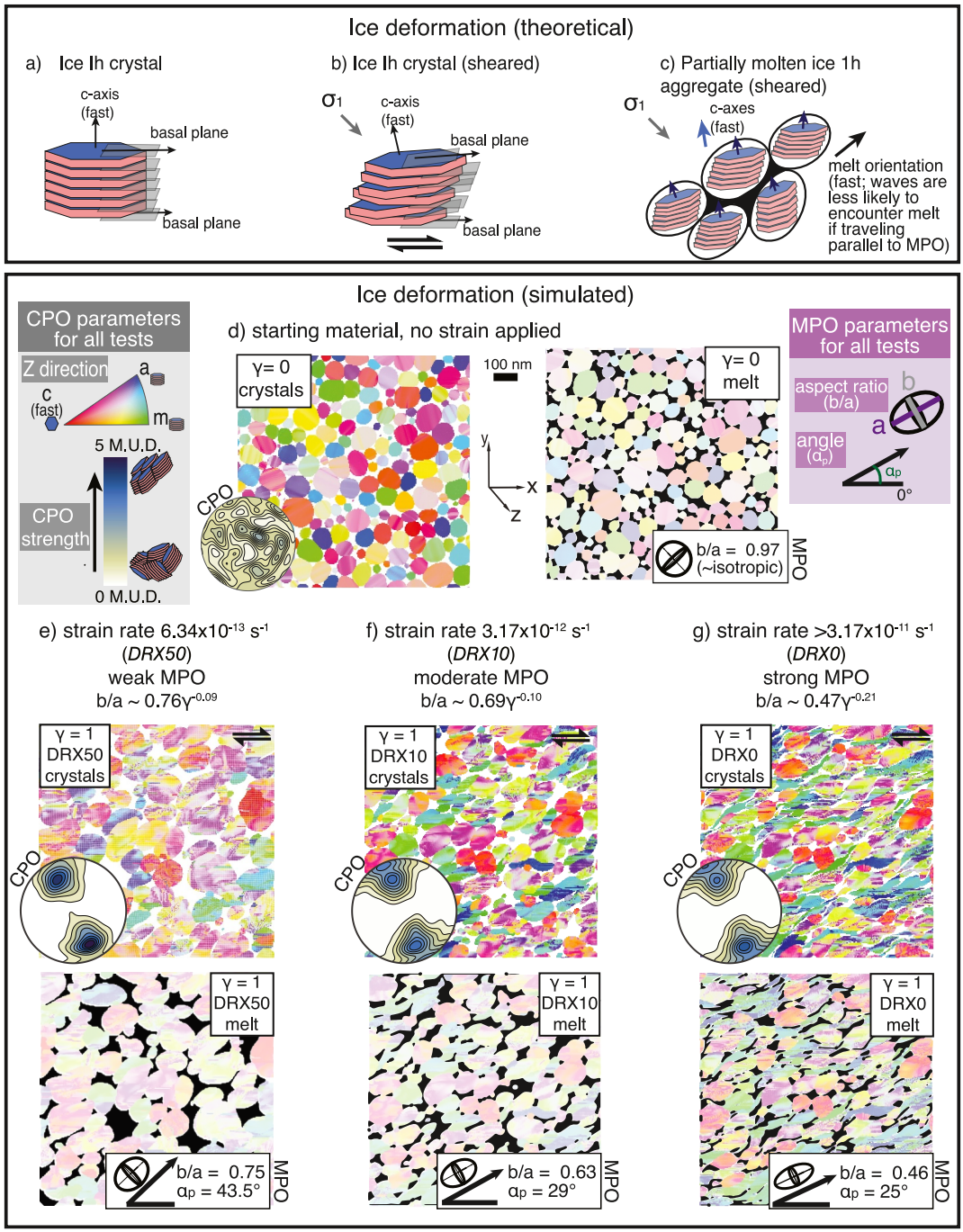

Figure 1. Theoretical and simulated deformation of ice aggregates. *Top box*: Schematic illustration of crystallographic preferred orientation (CPO) and melt preferred orientation (MPO) formation during ice deformation, including (a) an ice-Ih crystal prior to deformation, (b) a sheared ice-Ih crystal where deformation is accommodated primarily along the basal plane, and (c) a sheared ice-melt aggregate with c-axis alignment and MPO labeled. *Bottom box*: Microstructures from deformation simulations showing evolution of CPO and MPO as a function of dynamic recrystallization (DRX) rate, for 16% 2D melt. Each simulation microstructure has brightly colored ice grains in one image (left in panel (d), top in panels (e, f, g)), and black colored melt in a second image (right in panel (d), bottom in panels (e, f, g)) from the same step of the simulation. Ice grains are colored according to crystal axes parallel to *Z*-direction. Ice c-axis pole figures are plotted as equal-area, lower-hemisphere projections, where color intensity indicates CPO strength in multiples of uniform distribution (M.U.D.). MPO is defined by the average aspect ratio of the long and short axes (a and b, respectively) of ellipses fit to each isolated melt pocket, and the mean long axis orientation (α_p).

models (Joughin et al., 2012). Furthermore, logistical and safety issues prohibit drilling to obtain cores for CPO measurement in sites of fast-flowing ice (Lutz et al., 2022) including outlet glaciers and ice streams that are the major conduits for ice sheet discharge (e.g., Rignot et al., 2011). Other constraints on ice sheet anisotropy are required. To this end, indirect measurements of ice CPO are increasingly being obtained from both active- (Horgan et al., 2012; Picotti et al., 2015) and passive-source seismic sensing (Kufner et al., 2023; Scambos et al., 2017; Wittlinger & Farra, 2012, 2015), distributed acoustic sensing (Booth et al., 2020), and surface-deployed and airborne radar (Brisbourne et al., 2019; Fujita et al., 2000; Jordan et al., 2022; Matsuoka et al., 2003; Siegert & Kwok, 2000). Due to the elastic and dielectric anisotropy of ice, depth-resolved changes in CPO are often inferred from measurements of seismic anisotropy (e.g., Blankenship & Bentley, 1987; Kufner et al., 2023), radar anisotropy (e.g., Dall, 2010) and englacial seismic and radar reflections (e.g., Horgan et al., 2012; Siegert & Kwok, 2000). Such changes are often attributed to the effects of strain, impurities, and temperature, all of which are known to influence ice CPO (e.g., Fan et al., 2020; Paterson, 1991).

However, it is now well established for olivine, another mineral with strong viscous anisotropy, that CPO and seismic anisotropy can be modified by the presence of melt (Holtzman et al., 2003). For example, Heidelbach et al. (2005) showed that melt-bearing olivine samples deform via different dislocation slip systems compared to melt-free samples, producing a 90° rotation of the seismic fast direction. Given the distinct seismic, dielectric, and rheologic properties of solid and liquid phases, melt preferred orientation (MPO; Figure 1) can also modify geophysical signals usually attributed to CPO alone (Katz & Takei, 2013; Seltzer et al., 2023; Taylor-West & Katz, 2015). For instance, Seltzer et al. (2023) recently found that MPO evolves more quickly than CPO in partially molten olivine aggregates, suggesting that changes to seismic anisotropy in response to transient deformation can be attributed to melt rather than solid orientations. Given the ubiquity of temperate ice across the Greenland and Antarctic ice sheets—particularly in regions of fast-flowing ice (e.g., Meyer & Minchew, 2018) including basal ice—it is important to consider how MPO might impact geophysical interpretations of ice sheet anisotropy over the observational period of scientific studies.

Here, we used numerical simulations to assess the influence of MPO on seismic anisotropy within temperate ice. Simulations were performed using a viscoplastic full-field transform (VPFFT) approach within the ELLE platform (Piazolo et al., 2010). This work directly builds upon previous research by Llorens et al. (2020), which used ELLE simulations to examine the effect of melt volume alone on CPO-induced seismic anisotropy in temperate ice. We extend their findings by examining the role of MPO development. MPO was varied by changing the effective rate of dynamic recrystallization, which governs grain boundary morphology and therefore melt inclusion shape. We find that MPO significantly affects the direction and magnitude of seismic anisotropy, especially at elevated strain rates, and discuss implications for geophysical surveying of glaciers and ice sheets.

2. Methods

2.1. Deformation Simulations

We used the numerical simulation platform ELLE (Piazolo et al., 2010) to model the evolving microstructure of ice aggregates including interstitial liquid water. The ELLE approach (Bons et al., 2008) is rooted in the integration of a comprehensive viscoplastic model using a Fast Fourier Transform algorithm (VPFFT; Lebensohn & Rollett, 2020). The VPFFT formulation allows us to resolve stress and strain rate fields that minimize the average local work rate while adhering to compatibility and equilibrium constraints. To facilitate this, we calculated geometrically necessary dislocation densities and deformation-induced lattice rotation by integrating velocity gradient fields provided by VPFFT over time. Dynamic recrystallization (DRX) was modeled through the combined effects of grain boundary migration, recovery, and nucleation. Llorens et al. (2020) contains a complete description and parameters involved in the DRX modules applied here. Within this numerical setup, the water phase was treated as an effectively isotropic, viscous material with a stiffness approaching zero, resembling the properties of an amorphous liquid.

All simulations were performed in dextral simple shear, with shear strain increments of $\gamma = 0.02$, up to a final strain of $\gamma = 2.5$, in order to survey the importance of MPO well beyond the point of CPO establishment ($\gamma \lessapprox 1$; Qi et al., 2019). The simulations also imposed four different *DRX* rates, with either 0, 1, 10, or 50 steps of *DRX* per deformation increment. These values correspond inversely to strain rate, such that high-*DRX* simulations were able to retain shape between increments and therefore experienced the lowest effective strain rates: Simulations with 50 *DRX* steps had effective strain rates of 6.34×10^{-13} s^{-1}, those with 10 *DRX* steps had 3.17×10^{-12} s^{-1},

those with 1 step had strain rates of 3.17×10^{-11} s^{-1}, and those without any *DRX*, which do not include time in the model, can be considered analogous to strain rates $>3.17 \times 10^{-11}$ s^{-1}. The degree of *DRX* and, therefore, the strain rate, did not significantly affect orientation of the CPO (Figure S2 in Supporting Information S1). Instead, *DRX* acted as a proxy for MPO (Figures 1e–1g; Figure S1 in Supporting Information S1) as it modifies the shape and distribution of ice-ice and ice-melt grain boundaries following the reduction of the surface energy and stored strain energy (see further discussion of the effect of *DRX* on morphology in Llorens et al., 2019).

2.2. Anisotropy Calculations

MPO strength was defined using the particle orientation (PAROR) method of Heilbronner and Barrett (2014, chapter 14). A convex hull was fit to each individual melt pocket, from which we calculated the non-elliptical long axis, a, short axis, b, and long axis orientation, α_p (Figure 1). MPO strength is given by the ratio b/a, while MPO orientation is given as the average value of α_p (following Seltzer et al., 2023). We calculated seismic anisotropy at each deformation increment using a poroelastic differential effective medium method (Gassman, 1951; Kim et al., 2019) whereby an effective Voigt stiffness tensor is calculated from the integrated elastic properties of the crystalline ice matrix. This method calculates the elastic constants of a melt-ice aggregate by mathematically treating all melt as a single fluid-filled crack of aspect ratio b/a, with average orientation given by α_p. For comparison, we also calculated an effective stiffness tensor assuming isotropically oriented melt, where $b/a = 1$.

2.3. Projection to 3D

We simulated the deformation of ice containing 0%, 7%, and 16% 2D melt. These non-zero values are higher than the expected melt volume of temperate ice (possibly up to 8%; Haseloff et al., 2019), because the ELLE toolbox uses a pseudo-3D geometry, where a 2D microstructure is projected uniformly into 3D. Scaling from 2D to 3D is not straightforward due to stereological effects (von Bargen & Waff, 1986). Laboratory thin sections frequently have 2D melt fractions 1–2 times greater than the known 3D melt content (e.g., Seltzer et al., 2023; Zimmerman et al., 1999); accordingly, we computed all 3D tensors using three melt scaling fractions: ½, ¾, and 1. All results presented in the main text are created using the ½ scaling fraction as it is the most conservative estimate, corresponding to 0, 3.5, and 8 vol.% melt. Complementary figures using higher melt scaling fractions can be found in Supporting Information S1.

We assume that the 2D melt represents a cross section of a penny-shaped ellipsoid between grains, such that the b/a ratio defined by the PAROR method (see previous section) corresponds to an ellipsoid with axis lengths 1:b/a:1 (Faul et al., 1994).

3. Results

3.1. Anisotropy From Simulated MPOs

With increasing strain, MPO strength increases as grains become flattened and elongated (Figures 1e–1g, Figure S3 in Supporting Information S1). MPO evolution also becomes more pronounced as the rate of dynamic recrystallization, *DRX*, decreases (see Figure S1 in Supporting Information S1 for a quantitative analysis). At high DRX values (low effective strain rates), grain boundary migration enables grains to retain roughly equant shapes (Figure 1e). However, as the DRX value decreases (effective strain rate increases), lattice rotation and grain elongation dominate, producing flattened grain shapes and interconnected melt bands inclined ~20° antithetic to the shear direction (Figure 1g).

Regardless of melt content and MPO strength, the CPO and seismic anisotropy of the solid ice matrix remains constant. Ice c-axes align sub-normal to the shear direction (see pole figures in Figure 1) as deformation is primarily accommodated by slip on the (0001) basal plane, as observed in shear experiments (e.g., Qi et al., 2019). Without melt (Figures 2a and 2d)—and even with relatively large volumes of isotropic (randomly oriented) melt (Figure 2e)—the P-wave fast axis aligns parallel with the ice c-axis, normal to the shear plane. However, the addition of 3.5% oriented melt rotates the P-wave fast axis ~90° toward the shear direction (Figures 2c and 2f). Meanwhile, the polarization direction of the fastest S-wave (S_1), the "fast direction" commonly used to infer the orientation of ice c-axes, also rotates ~90° with the addition of MPO, becoming aligned sub-parallel with the shear direction (Figure 2, rightmost column).

10.1029/2024GL110131

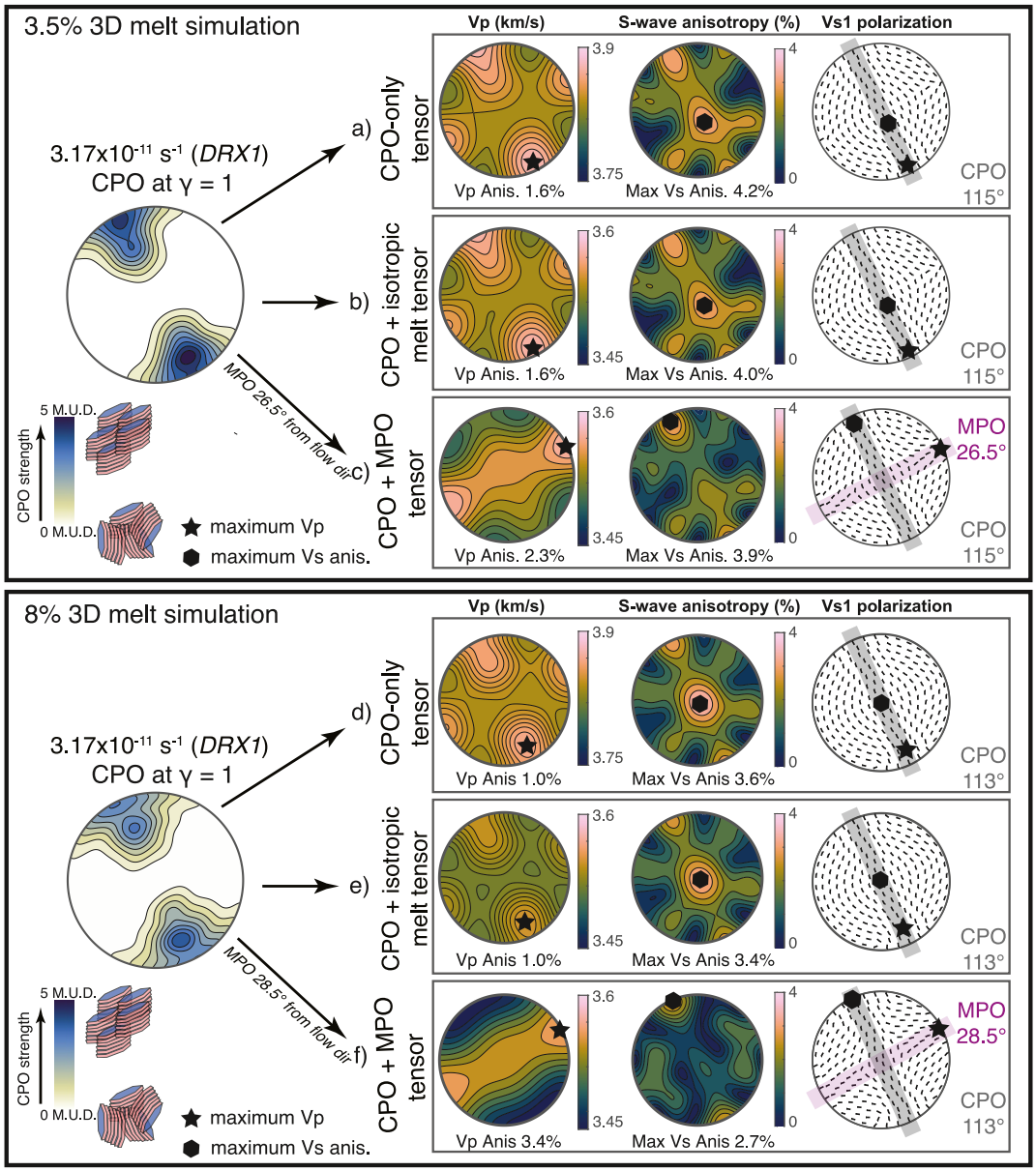

Figure 2. Vp and Vs anisotropies, and polarization of fast S-waves (S_1), for a 3.5 vol.% melt simulation (a, b, c) and 8 vol.% melt simulation (d, e, f), sheared to $\gamma = 1$ at a strain rate of 3.17×10^{-11} s^{-1}. Crystallographic preferred orientation (CPO) is represented as a contoured c-axis pole figure on the left (upper-hemisphere, equal-area projection), representing the orientation of the seismically fast c-axes. Anisotropy is calculated using (a), (d) only CPO of solid ice matrix, (b), (e) ice CPO with isotropic (randomly oriented) melt, and (c), (f) ice CPO with the actual MPO from the simulation, aligned 26.5° (3.5% melt) and 28.5° (8% melt) antithetic to shear plane. Note changes to color bars between (a), (d) and (b, c, e, f): the introduction of melt reduces velocities such that a single colorscale obscures distribution of Vp. Polarization direction (far right) depicts the polarization of S_1. CPO (c-axis cluster) angle is highlighted in gray, and MPO angle is highlighted in purple in panels (c), (f). The location of maximum Vp is highlighted with a star, and the location of maximum vs. anisotropy highlighted with a hexagon.

MPO also changes the maximum degree of seismic anisotropy in a deforming aggregate, especially when melt fractions and MPO strengths are high. When the MPO and CPO are not co-aligned, as in these simulations, stronger MPOs reduce S-wave anisotropy. The lowest-strain-rate, highest-*DRX* simulations exhibit increased CPO strength compared to other simulations (Figures S6a and S7a in Supporting Information S1), and so elevated seismic anisotropy from CPO alone (Figures S4b and S5b in Supporting Information S1). Nevertheless, seismic

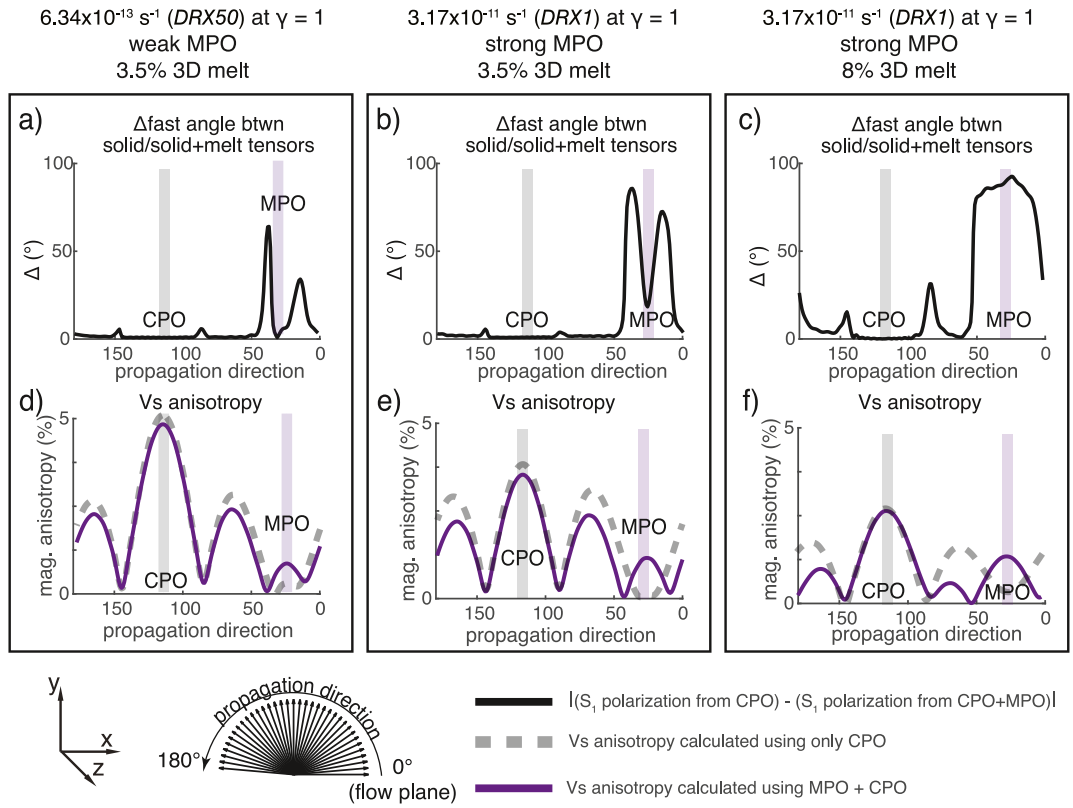

Figure 3. MPO-dependent changes to observed fast direction and magnitude of anisotropy as a function of wave propagation direction through the 2D plane of the simulation, where 90° is vertical and 0° is horizontal to the right. MPO and c-axis orientation are marked with gray and purple bars, respectively, on each plot. (a, b, c) Magnitude of difference between polarization of fastest S-wave between CPO-only elastic tensor and MPO-inclusive tensor, as a function of wave propagation direction, for (a) low-melt, weak-MPO simulation, (b) low-melt, strong-MPO simulation, and (c) high-melt, strong-MPO simulation. (d, e, f) Vs anisotropy as a function of propagation direction for CPO-only tensors (gray dashed line) and crystallographic preferred orientation + MPO tensors (purple solid line).

anisotropy increased with strain above the CPO saturation point at $\gamma = 0.5$–0.75 in melt-bearing simulations. This increase can be attributed to MPO strengthening at higher strains.

To further explore how MPO affects the geophysical properties of temperate ice, we calculated the difference between the S_1 polarization direction of a melt-free tensor and a tensor including MPO (Figures 3a–3c). The fast direction calculated from the two tensors is never the same (there is always some non-zero rotation), and can rotate by nearly 90° when waves travel near the MPO; the maximum rotations for 3.5% melt are >85° for all simulations except those with the lowest strain rate and weakest MPO (maximum rotation of 64°; Figure S4 in Supporting Information S1).

To demonstrate the effect of MPO on Vs anisotropy, we also calculated the magnitude of Vs anisotropy, ΔVs, for a range of propagation directions in the plane containing the shear direction and shear-plane-normal (Figures 3d–3f). For most S-wave propagation directions, ΔVs is reduced by the addition of MPO (Figures 3d–3f: note how the purple, CPO + MPO curves give generally lower values of ΔVs compared to the gray, CPO-only curves). Only when S-waves are traveling within ∼20° of the MPO does ΔVs increase relative to the CPO-only models. The magnitude of this change to S-wave anisotropy varies as function of both MPO strength and melt fraction (Figures S4 and S5 in Supporting Information S1). Furthermore, relative increases in Vs anisotropy along the MPO direction are dependent on the strength of the MPO. For 3.5 vol.% melt, there is a 3.5× increase in Vs anisotropy along MPO direction in a strong-MPO, low-*DRX* case, versus a 2.3× increase in Vs anisotropy along MPO direction for weak-MPO, high-*DRX* case (Figures 3d and 3e; Figure S4 in Supporting Information S1). Vs anisotropies for waves traveling parallel to the MPO can match or exceed those of waves traveling parallel to CPO if higher degrees of 2D → 3D melt scaling are used (Figure S5 in Supporting Information S1).

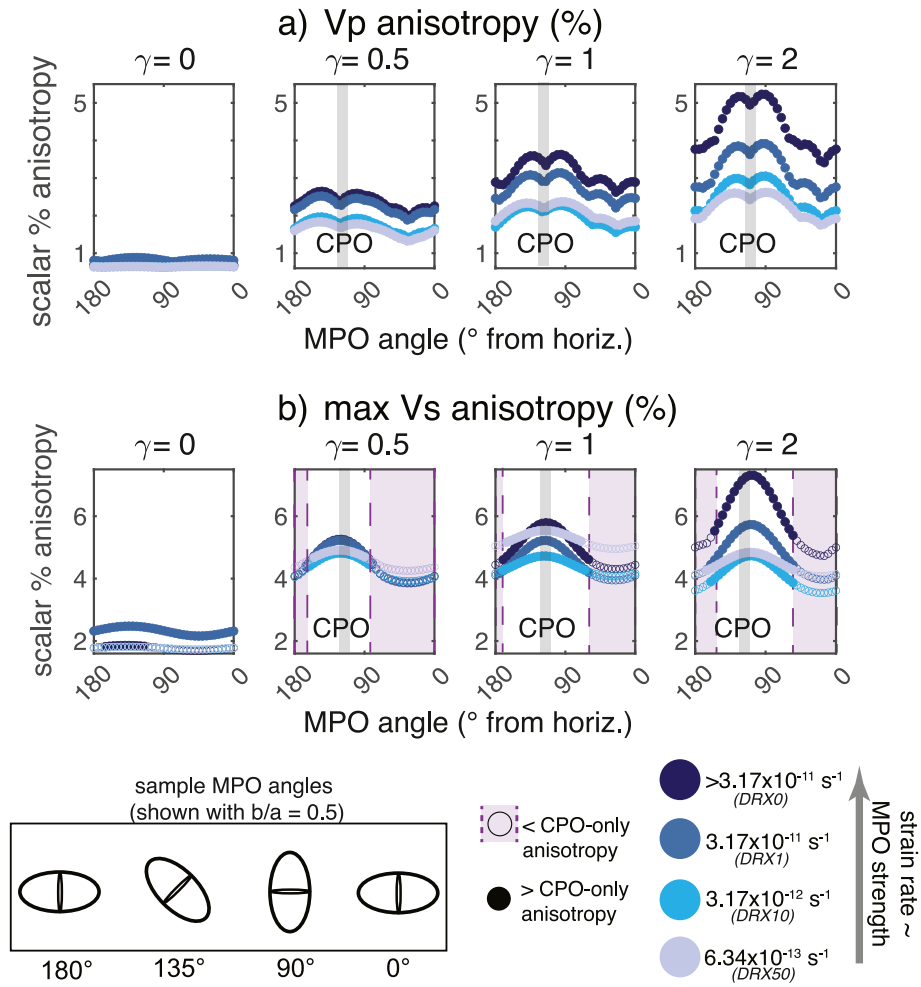

Figure 4. Effects of MPO rotation on calculated anisotropy. Each plot shows calculated values using crystallographic preferred orientation (CPO) from the simulations, artificially rotating the MPO from the flow plane, 0°, in intervals of 5°. In all $\gamma > 0$, the CPO angle is established at 110–120° from the horizontal shear plane, indicated with a gray bar. Markers correspond to strain rates and therefore MPO strength, and show whether the test produced scalar anisotropies higher (filled dot) or lower (open dot) than the CPO-only value. MPO angles yielding anisotropy lower than CPO-only anisotropy are shaded in purple, except in $\gamma = 0$ simulation, where neither MPO nor CPO are strong. No tests had identical anisotropy values to the corresponding CPO-only predictions. (a) Absolute Vp anisotropy as a function of theoretical MPO angle and strain, (b) Maximum absolute Vs anisotropy as a function of theoretical MPO angle and strain.

3.2. Interaction Between MPO and CPO in Generating Seismic Anisotropy

To explore how MPO angle impacts seismic anisotropy, we artificially rotated the MPO at preferred angles from 0 to 175° while keeping the CPO constant (Figure 4). As MPO rotates toward the c-axis maximum direction (~115°), both Vp anisotropy and Vs anisotropy increase (Figures 4a and 4b, respectively). This is expected; the MPO contributes an additional fast direction, so co-alignment enhances the CPO-related fast direction. Conversely, Vp and Vs anisotropies are lowest when the melt is oriented at ~90° from the CPO direction, as the MPO fast direction counteracts the CPO-generated fast direction.

Regardless of the orientation and strength of the MPO, seismic anisotropy values from MPO rotation testing are never equivalent to CPO-only anisotropy. Vp and Vs anisotropy generally increase as the MPO strengthens with increasing strain and strain rate (although weak-MPO simulations retain strong CPO-generated anisotropy, as discussed in the previous section, which is still modified by increasing MPO strength at higher strains). Vp anisotropy is almost uniformly higher than CPO-only values no matter the MPO (Figure 4a), while the addition of melt to the CPO tensor enhances Vs anisotropy depending on degree of strain and strain/*DRX* rate. At $\gamma = 0.5$, around the point of CPO establishment, MPO increases Vs anisotropy when MPO and CPO align within 40° of

one another. At $\gamma = 2$, MPO increases CPO-induced Vs anisotropy when MPO and CPO are aligned within 55° (Figure 4b).

The absolute reduction in seismic wavespeeds depends on both the melt percentage (Figures S8–S10 in Supporting Information S1) and also the MPO strength and orientation. Changes from the CPO-only value are highest at MPOs near the direction of flow, 70–100° from the CPO fast direction. These effects are enhanced at higher values of 2D → 3D melt scaling (Figures S9 and S10 in Supporting Information S1).

4. Discussion

Our models indicate that MPO will always modify the CPO-induced seismic anisotropy of temperate ice, such that seismic anisotropy arises from the combined effects of both melt and crystalline components. While previous computational studies reported that 15% 2D melt was required to obscure the signal of a CPO (Llorens et al., 2020; this study also contained a discussion of meltwater's effects on CPO), we find that much lower degrees of melt (≤7% 2D melt = 3.5 vol.% 3D melt) can significantly change the seismic properties of temperate ice. This volume of oriented melt can rotate seismic fast directions by 90°, enhance the degree of Vp anisotropy by up to 110% (≤54% with the weakest studied MPO at $\gamma \geq 0.5$), and either enhance the degree of maximum Vs anisotropy by up to 36% or decrease it by up to 9% (depending on the relative orientation of melt and crystals). Geophysical studies of temperate ice that only account for CPO are therefore likely to significantly overpredict the magnitude of ice flow based on Vp anisotropy, or to either over- or under-predict ice flow magnitude from Vs anisotropy. At modeled strain rates $\geq 3.17 \times 10^{-12}$ s^{-1} ($DRX \leq 10$), comparable to those estimated at the base of cores from the Greenland ice sheet (Montagnat et al., 2014) and fast-flowing regions across Antarctica (Ranganathan & Minchew, 2024), the effect of MPO is particularly heightened. We suggest that MPO should prominently affect seismic and radar anisotropy in temperate, fast-flowing icy settings that are the primary drivers of solid ice discharge.

While CPO-only models may under- or overpredict the magnitude of temperate ice flow, as well as potentially misrepresent the direction of flow, MPO-modified seismic anisotropy may still relate consistently to the direction of flow. If melt aligns in a predictable direction with regards to the direction of applied stress (sub-parallel with the shear direction), as has recently been observed in the olivine-basalt system (Seltzer et al., 2023), the seismic fast direction may track the stress field rather than the orientation of c-axes. Compressive tests by Wilson et al. (2024) do suggest that deuterized melt inclusions orient subparallel to the maximum local shear stress, supporting the idea that meltwater inclusions track local stress fields. Alignment at ∼135°, matching the maximum principal stress in our simulations, would enhance CPO-generated P-wave anisotropy (by 34%–100% at $\gamma = 0.5$ and 53%–108% at $\gamma = 2$) and S-wave anisotropy (by 5%–20% at $\gamma = 0.5$ and by 11%–30% at $\gamma = 2$) (Figure 4), potentially leading to overestimates of CPO generation and therefore ice flow. Laboratory shear experiments that characterize the microstructural evolution of meltwater inclusion in icy aggregates are therefore necessary to refine expectations for melt orientations in sheared ice, and to improve dynamics of melt in experimental simulation models like ELLE.

5. Conclusions

We simulated the deformation of temperate ice and calculated the relative importance of melt preferred orientations (MPO) on generating seismic anisotropy. Small percentages of melt (3.5 vol.%) affected the magnitude and orientation of anisotropy, rotating the Vp fast direction and polarization direction of fast S waves toward the MPO regardless of strength of MPO orientation. These rotations can be up to 90° from fast polarizations created by solid ice alone. The effects of MPO become particularly pronounced at strain rates $\geq 3.17 \times 10^{-12}$ s^{-1}. This suggests that geophysical studies of temperate glacial settings require caution when inferring flow directions or ice flow enhancement (i.e., CPO strength): stronger CPO does not correspond uniformly to higher magnitudes of anisotropy if MPO is present, especially when flow is relatively fast (as is common for temperate ice). Neglecting the role of melt may lead to an overprediction of CPO strength by up to 110% based on Vp anisotropy, and therefore to significant overestimation of flow magnitude. Conversely, the presence of MPO can cause underpredictions of flow magnitudes by up to 9% based on Vs anisotropy. MPO must therefore be considered when conducting geophysical surveys to constrain polar ice flow for models of ice mass loss and sea level rise.

Data Availability Statement

ELLE output files and microstructural melt images for every simulation considered in this paper are available for download via Zenodo at https://doi.org/10.5281/zenodo.10637171 (Seltzer, 2024). These files were combined with the publicly available GassDEM code (Kim et al., 2019) using parameters outlined in Methods section and Supporting Information S1.

Acknowledgments
Thank you to Joanna Millstein, Nori Nakata, and Matěj Peč for feedback. Thank you to Dr. Sheng Fan and two anonymous reviewers for helpful, constructive commentary on the manuscript. Figures were plotted using perceptually uniform colormaps from Crameri (2021). CS received support from the MathWorks MIT School of Science Fellowship. MGL acknowledges the "Consolidación Investigadora" Grant CNS3022-135819 funded by Ministerio de Ciencia e Innovación/Agencia Estatal de Investigación/10.13039/501100011033 and EU NextGenerationEU/PRTR. AJC was supported by a National Science Foundation award, OPP-2317263.

References

Azuma, N., & Higashi, A. (1985). Formation processes of ice fabric pattern in ice sheets. *Annals of Glaciology*, *6*, 130–134. https://doi.org/10.3189/1985AoG6-1-130-134

Bamber, J. L., Oppenheimer, M., Kopp, R. E., Aspinall, W. P., & Cooke, R. M. (2019). Ice sheet contributions to future sea-level rise from structured expert judgment. *Proceedings of the National Academy of Sciences of the United States of America*, *116*(23), 11195–11200. https://doi.org/10.1073/pnas.1817205116

Blankenship, D., & Bentley, C. (1987). *The crystalline fabric of polar ice sheets inferred from seismic anisotropy, The Physical Basis of Ice Sheet Modeling*. International Association of Hydrological Sciences Press, Institute of Hydrology.

Bons, P. D. D., Koehn, D., & Jessell, M. W. (Eds.) (2008)., *Microdynamics simulation, lecture notes in Earth sciences*. Springer. https://doi.org/10.1007/978-3-540-44793-1

Booth, A. D., Christoffersen, P., Schoonman, C., Clarke, A., Hubbard, B., Law, R., et al. (2020). Distributed acoustic sensing of seismic properties in a borehole drilled on a fast-flowing Greenlandic outlet glacier. *Geophysical Research Letters*, *47*(13), e2020GL088148. https://doi.org/10.1029/2020GL088148

Brisbourne, A. M., Martín, C., Smith, A. M., Baird, A. F., Kendall, J. M., & Kingslake, J. (2019). Constraining recent ice flow history at Korff ice rise, west Antarctica, using radar and seismic measurements of ice fabric. *J. Geophys. Res.Earth Surface*, *124*(1), 175–194. https://doi.org/10.1029/2018JF004776

Crameri, F. (2021). Scientific colour maps. https://doi.org/10.5281/zenodo.5501399

Dall, J. (2010). Ice sheet anisotropy measured with polarimetric ice sounding radar. In *Presented at the IGARSS 2010 - 2010 IEEE international geoscience and remote sensing symposium* (pp. 2507–2510). IEEE. https://doi.org/10.1109/IGARSS.2010.5653528

Duval, P., Ashby, M. F., & Anderman, I. (1983). Rate-controlling processes in the creep of polycrystalline ice. *Journal of Physical Chemistry*, *87*(21), 4066–4074. https://doi.org/10.1021/j100244a014

Edwards, T. L., Nowicki, S., Marzeion, B., Hock, R., Goelzer, H., Seroussi, H., et al. (2021). Projected land ice contributions to twenty-first-century sea level rise. *Nature*, *593*(7857), 74–82. https://doi.org/10.1038/s41586-021-03302-y

Fan, S., Cross, A. J., Prior, D. J., Goldsby, D. L., Hager, T. F., Negrini, M., & Qi, C. (2021). Crystallographic preferred orientation (CPO) development governs strain weakening in ice: Insights from high-temperature deformation experiments. *Journal of Geophysical Research: Solid Earth*, *126*(12), e2021JB023173. https://doi.org/10.1029/2021JB023173

Fan, S., Hager, T. F., Prior, D. J., Cross, A. J., Goldsby, D. L., Qi, C., et al. (2020). Temperature and strain controls on ice deformation mechanisms: Insights from the microstructures of samples deformed to progressively higher strains at −10, −20 and −30°C. *The Cryosphere*, *14*(11), 3875–3905. https://doi.org/10.5194/tc-14-3875-2020

Faria, S. H., Weikusat, I., & Azuma, N. (2014). The microstructure of polar ice. Part I: Highlights from ice core research. *Journal of Structural Geology, Microdynamics of Ice*, *61*, 2–20. https://doi.org/10.1016/j.jsg.2013.09.010

Faul, U. H., Toomey, D. R., & Waff, H. S. (1994). Intergranular basaltic melt is distributed in thin, elogated inclusions. *Geophysical Research Letters*, *21*(1), 29–32. https://doi.org/10.1029/93GL03051

Fujita, S., Matsuoka, T., Ishida, T., Matsuoka, K., & Mae, S. (2000). A summary of the complex dielectric permittivity of ice in the megahertz range and its applications for radar sounding of polar ice sheets. *Phys. Ice Core Rec.*, 185–212.

Gassman, F. (1951). Uber die Elastizitat Poroser Medien. *Vierteljahrsschrift der Naturforschende Gesellschaft in Zürich*, *96*, 1–23.

Haseloff, M., Hewitt, I. J., & Katz, R. F. (2019). Englacial pore water localizes shear in temperate ice stream margins. *J. Geophys. Res.Earth Surface*, *124*(11), 2521–2541. https://doi.org/10.1029/2019JF005399

Heidelbach, F., Holtzman, B., Hier-Majumder, S., & Kohlstedt, D. (2005). Textures in experimentally deformed olivine aggregates: The effects of added water and melt. *Materials Science Forum*, *495–497*, 63–68. https://doi.org/10.4028/www.scientific.net/MSF.495-497.63

Heilbronner, R., & Barrett, S. (2014). Particle fabrics. In *Image analysis in Earth sciences* (pp. 253–281). Springer. https://doi.org/10.1007/978-3-642-10343-8_14

Holtzman, B. K., Kohlstedt, D. L., Zimmerman, M. E., Heidelbach, F., Hiraga, T., & Hustoft, J. (2003). Melt segregation and strain partitioning: Implications for seismic anisotropy and mantle flow. *Science*, *301*(5637), 1227–1230. https://doi.org/10.1126/science.1087132

Horgan, H. J., Anandakrishnan, S., Jacobel, R. W., Christianson, K., Alley, R. B., Heeszel, D. S., et al. (2012). Subglacial Lake Whillans — Seismic observations of a shallow active reservoir beneath a West Antarctic ice stream. *Earth and Planetary Science Letters*, *331–332*, 201–209. https://doi.org/10.1016/j.epsl.2012.02.023

Jordan, T. M., Martín, C., Brisbourne, A. M., Schroeder, D. M., & Smith, A. M. (2022). Radar characterization of ice crystal orientation fabric and anisotropic viscosity within an Antarctic ice stream. *J. Geophys. Res.Earth Surface*, *127*(6), e2022JF006673. https://doi.org/10.1029/2022JF006673

Joughin, I., Alley, R. B., & Holland, D. M. (2012). Ice-sheet response to oceanic forcing. *Science*, *338*(6111), 1172–1176. https://doi.org/10.1126/science.1226481

Katz, R. F., & Takei, Y. (2013). Consequences of viscous anisotropy in a deforming, two-phase aggregate. Part 2. Numerical solutions of the full equations. *Journal of Fluid Mechanics*, *734*, 456–485. https://doi.org/10.1017/jfm.2013.483

Kim, E., Kim, Y., & Mainprice, D. (2019). GassDem: A MATLAB program for modeling the anisotropic seismic properties of porous medium using differential effective medium theory and Gassmann's poroelastic relationship. *Computational Geosciences*, *126*, 131–141. https://doi.org/10.1016/j.cageo.2019.02.008

Kufner, S.-K., Wookey, J., Brisbourne, A. M., Martín, C., Hudson, T. S., Kendall, J. M., & Smith, A. M. (2023). Strongly depth-dependent ice fabric in a fast-flowing Antarctic ice stream revealed with icequake observations. *J. Geophys. Res.Earth Surface*, *128*(3), e2022JF006853. https://doi.org/10.1029/2022JF006853

Lebensohn, R. A., & Rollett, A. D. (2020). Spectral methods for full-field micromechanical modelling of polycrystalline materials. *Computational Materials Science*, *173*, 109336. https://doi.org/10.1016/j.commatsci.2019.109336

Li, D., DeConto, R. M., & Pollard, D. (2023). Climate model differences contribute deep uncertainty in future Antarctic ice loss. *Science Advances*, *9*(7), eadd7082. https://doi.org/10.1126/sciadv.add7082

Llorens, M.-G., Gomez-Rivas, E., Ganzhorn, A.-C., Griera, A., Steinbach, F., Roessiger, J., et al. (2019). The effect of dynamic recrystallisation on the rheology and microstructures of partially molten rocks. *Journal of Structural Geology*, *118*, 224–235. https://doi.org/10.1016/j.jsg.2018.10.013

Llorens, M.-G., Griera, A., Bons, P. D., Gomez-Rivas, E., Weikusat, I., Prior, D. J., et al. (2020). Seismic anisotropy of temperate ice in polar ice sheets. *J. Geophys. Res.Earth Surface*, *125*(11), e2020JF005714. https://doi.org/10.1029/2020JF005714

Lutz, F., Prior, D. J., Still, H., Bowman, M. H., Boucinhas, B., Craw, L., et al. (2022). Ultrasonic and seismic constraints on crystallographic preferred orientations of the Priestley Glacier shear margin, Antarctica. *The Cryosphere*, *16*(8), 3313–3329. https://doi.org/10.5194/tc-16-3313-2022

Matsuoka, K., Furukawa, T., Fujita, S., Maeno, H., Uratsuka, S., Naruse, R., & Watanabe, O. (2003). Crystal orientation fabrics within the Antarctic ice sheet revealed by a multipolarization plane and dual-frequency radar survey. *Journal of Geophysical Research*, *108*(B10). https://doi.org/10.1029/2003JB002425

Meyer, C. R., & Minchew, B. M. (2018). Temperate ice in the shear margins of the Antarctic Ice Sheet: Controlling processes and preliminary locations. *Earth and Planetary Science Letters*, *498*, 17–26. https://doi.org/10.1016/j.epsl.2018.06.028

Montagnat, M., Azuma, N., Dahl-Jensen, D., Eichler, J., Fujita, S., Gillet-Chaulet, F., et al. (2014). Fabric along the NEEM ice core, Greenland, and its comparison with GRIP and NGRIP ice cores. *The Cryosphere*, *8*(4), 1129–1138. https://doi.org/10.5194/tc-8-1129-2014

Oppenheimer, M., Glavovic, B., Hinkel, J., van de Wal, R., Magnan, A. K., Abd-Elgawad, A., et al. (2019). Sea level rise and implications for low lying islands, coasts and communities.

Paterson, W. S. B. (1991). Why ice-age ice is sometimes "soft". *Cold Regions Science and Technology*, *20*(1), 75–98. https://doi.org/10.1016/0165-232X(91)90058-O

Piazolo, S., Jessell, M. W., Bons, P. D., Evans, L., & Becker, J. K. (2010). Numerical simulations of microstructures using the Elle platform: A modern research and teaching tool. *Journal of the Geological Society of India*, *75*(1), 110–127. https://doi.org/10.1007/s12594-010-0028-6

Picotti, S., Vuan, A., Carcione, J. M., Horgan, H. J., & Anandakrishnan, S. (2015). Anisotropy and crystalline fabric of Whillans Ice Stream (West Antarctica) inferred from multicomponent seismic data. *Journal of Geophysical Research: Solid Earth*, *120*(6), 4237–4262. https://doi.org/10.1002/2014JB011591

Pimienta, P., Duval, P., & Lipenkov, V. Y. (1987). Mechanical behavior of anisotropic polar ice. *Physics Basis Ice Sheet Model*.

Qi, C., Prior, D. J., Craw, L., Fan, S., Llorens, M.-G., Griera, A., et al. (2019). Crystallographic preferred orientations of ice deformed in direct-shear experiments at low temperatures. *The Cryosphere*, *13*(1), 351–371. https://doi.org/10.5194/tc-13-351-2019

Ranganathan, M., & Minchew, B. (2024). A modified viscous flow law for natural glacier ice: Scaling from laboratories to ice sheets. *Proceedings of the National Academy of Sciences of the United States of America*, *121*(23), e2309788121. https://doi.org/10.1073/pnas.2309788121

Rignot, E., Mouginot, J., & Scheuchl, B. (2011). Ice flow of the Antarctic ice sheet. *Science*, *333*(6048), 1427–1430. https://doi.org/10.1126/science.1208336

Scambos, T. A., Bell, R. E., Alley, R. B., Anandakrishnan, S., Bromwich, D. H., Brunt, K., et al. (2017). How much, how fast? A science review and outlook for research on the instability of Antarctica's Thwaites Glacier in the 21st century. *Global and Planetary Change*, *153*, 16–34. https://doi.org/10.1016/j.gloplacha.2017.04.008

Seltzer, C. (2024). Supporting data for Melt inclusions control seismic anisotropy in deforming partially molten ice [Dataset]. https://doi.org/10.5281/zenodo.10637171

Seltzer, C., Peč, M., Zimmerman, M. E., & Kohlstedt, D. L. (2023). Melt network reorientation and crystallographic preferred orientation development in sheared partially molten rocks. *Geochemistry, Geophysics, Geosystems*, *24*(9), e2023GC010927. https://doi.org/10.1029/2023GC010927

Siegert, M. J., & Kwok, R. (2000). Ice-sheet radar layering and the development of preferred crystal orientation fabrics between Lake Vostok and Ridge B, central East Antarctica. *Earth and Planetary Science Letters*, *179*(2), 227–235. https://doi.org/10.1016/S0012-821X(00)00121-7

Taylor-West, J., & Katz, R. F. (2015). Melt-preferred orientation, anisotropic permeability and melt-band formation in a deforming, partially molten aggregate. *Geophysical Journal International*, *203*(2), 1253–1262. https://doi.org/10.1093/gji/ggv372

Treverrow, A., Budd, W. F., Jacka, T. H., & Warner, R. C. (2012). The tertiary creep of polycrystalline ice: Experimental evidence for stress-dependent levels of strain-rate enhancement. *Journal of Glaciology*, *58*(208), 301–314. https://doi.org/10.3189/2012JoG11J149

von Bargen, N., & Waff, H. S. (1986). Permeabilities, interfacial areas and curvatures of partially molten systems: Results of numerical computations of equilibrium microstructures. *Journal of Geophysical Research*, *91*(B9), 9261–9276. https://doi.org/10.1029/JB091iB09p09261

Wilson, C. J. L., Peternell, M., Salvemini, F., Luzin, V., Enzmann, F., Moravcova, O., & Hunter, N. J. R. (2024). Partial melting in polycrystalline ice: Pathways identified in 3D neutron tomographic images. *The Cryosphere*, *18*(2), 819–836. https://doi.org/10.5194/tc-18-819-2024

Wittlinger, G., & Farra, V. (2012). Observation of low shear wave velocity at the base of the polar ice sheets: Evidence for enhanced anisotropy. *Geophysical Journal International*, *190*(1), 391–405. https://doi.org/10.1111/j.1365-246X.2012.05474.x

Wittlinger, G., & Farra, V. (2015). Evidence of unfrozen liquids and seismic anisotropy at the base of the polar ice sheets. *Polar Science, Recent Advance in Polar Seismology: Global Impact of the International Polar Year*, *9*(1), 66–79. https://doi.org/10.1016/j.polar.2014.07.006

Zimmerman, M. E., Zhang, S., Kohlstedt, D. L., & Karato, S. (1999). Melt distribution in mantle rocks deformed in shear. *Geophysical Research Letters*, *26*(10), 1505–1508. https://doi.org/10.1029/1999GL900259

References From the Supporting Information

Becker, J. K., Bons, P. D., & Jessell, M. W., (2008). A new front-tracking method to model anisotropic grain and phase boundary motion in rocks. *Computational Geosciences*, *34*(3), 201-212. https://doi.org/10.1016/j.cageo.2007.03.013